Propagation of supersonic excitations through the carbon nanotube forest

L. Kh. Galiakhmetova[a,b], D. V. Bachurin[c], E. A. Korznikova[b,d], Igor A. Shepelev[a], and S. V. Dmitriev[b,e]

[a]Institute for Metals Superplasticity Problems, RAS, 450001 Ufa, Russia
[b]Institute of Molecule and Crystal Physics, UFRC, RAS, 450075 Ufa, Russia
[c]Institute for Applied Materials – Applied Materials Physics, Karlsruhe Institute of Technology, 76344 Eggenstein-Leopoldshafen, Germany
[d]Ufa State Aviation Technical University, 450008 Ufa, Russia
[e]Federal Research Center Institute of Applied Physics of RAS, 603950 Nizhny Novgorod, Russia

ABSTRACT

A beam of single-layer carbon nanotubes (CNTs) subjected to a shock load in the transverse direction was studied using a chain model with a reduced number of degrees of freedom. The compression shock wave is initiated by a piston moving at a constant speed. Two different scenarios of shock wave propagation and their influence on the structure of the CNT beam depending on the piston velocity were found. At lower speeds, only a faster wave front propagates, which leads to elliptization of the CNT, whereas at higher speeds this is accompanied by a slower wave front of collapse. The evolution of the CNT beam structure in time during compression is studied in detail. The energy absorption rate is estimated as a function of the piston velocity. The results obtained can be useful in the development of new types of elastic shock absorbers.

Keywords: Carbon nanotube forest, plane strain conditions, shock compression, deformation mechanisms, protection against shock and vibration

1. INTRODUCTION

Carbon nanotubes (CNTs) have excellent mechanical properties such as high Young's modulus ,[1] very high strength and energy absorption capacity .[2] CNTs are transparent [3] and good conductors of electricity [3–5] and heat .[6,7] The unique combination of properties makes CNTs very promising for the production of polymer composites with improved electrical and mechanical properties ,[8,9] supercapacitors ,[10,11] flexible and expandable electronic devices ,[3,12] composite materials [13] and many others.

Horizontally aligned CNT arrays can be obtained from vertically aligned CNT beams by pressing, drawing and rolling .[14–17] Single-wall CNT beams have linear elasticity up to a hydrostatic pressure of 1.5 GPa at room temperature and demonstrate a volumetric compressibility of 0.024 GPa^{-1} .[18] It is shown that the deformation of CNT beams under non-hydrostatic loading becomes irreversible at pressures greater than 5 GPa .[19] The results of experimental and numerical studies of the mechanical properties of CNTs have been summarized in .[20] The quasi-static lateral compression of CNTs and graphene has been analyzed, for example, in references. [21–26]

It is known from miniature ballistic tests at 600 m/s that the specific penetration energy for multilayer graphene is about 10 times higher than for macroscopic steel sheets .[27] The mechanical behavior of graphene

Further author information: (Send correspondence to S.V.D.)
L.K.G.: E-mail:
D.V.B.: E-mail: dmitry.bachurin@kit.edu
E.A.K.: E-mail: elena.a.korznikova@gmail.com
I.A.S.: E-mail: igor_sar@li.ru
S.V.D.: E-mail: dmitriev.sergey.v@gmail.com

under the action of silica and nickel nanoprojects moving at a speed of 5 km / s has been simulated, and a large amount of energy absorbed during deformation has been attributed to the excellent stress. and ultimate deformation of graphene .[28]

A modeling of the molecular dynamics of the collision of one, two and three layers of graphene with a rigid fullerene projectile was carried out for an impact speed between 3.5 and 7.5 km / s .[29] The appearance of two to three flat cracks in the graphene sheet was found. The impact dynamics of a fullerene molecule and a single-layered graphene sheet were investigated using an analytical approach based on non-local thin-plate theory and molecular dynamics .[30] The ability of a suspended graphene sheet to capture a single-walled carbon nanotube projectile was analyzed by Yang and Tong in .[31] In particular, the projectile has been shown to induce longitudinal and transverse wave fronts in graphene. As a result of such an impact, graphene absorbs 89-100% of the kinetic energy of the projectile. The latter means that graphene can efficiently trap nanoparticles or molecules at high speed. Plane shock waves in graphene and boron nitride have been analyzed by Shepelev .[32] The authors have shown that shock waves propagate over large distances in boron nitride relative to graphene and are associated with the diffusion of excitation energy by lattice phonons.

This work is devoted to the dynamic loading of two-dimensional materials, where a significant effect of the strain rate has been demonstrated. For example, in the experimental work ,[33] it was shown that when compressed by a shock wave, CNTs are much more damaged than under static compression. Graphene can absorb shock wave energy without interruption [34] or it can act as an intermediate layer to reflect shock waves .[35] The evolution of the structure of nanowires, fullerenes and nanotubes during a collision with an obstacle has been analyzed in the references. [30] A study of the penetration of an Ni projectile in multilayer graphene at an impact velocity of 900 m/s was carried out in the [36] with subsequent comparison with experimental data. The addition of CNT to the Kevlar fabric increases the resistance of epoxy composites to the penetration of steel shells.

2. MODEL

The dynamic uniaxial compression of a CNT zigzag beam under plane strain conditions is considered. The cross sections of the CNTs create a triangular network in the xy plane (see Fig. Link Fig. 1). Each carbon atom belonging to the cross section of an CNT is a member of a rigid chain of atoms perpendicular to the xy plane. ρ is the equilibrium interatomic distance in the zigzag CNT wall. $a = \rho\sqrt{3}/2$ - distance between neighboring atoms in projection on the xy plane. The number of atoms in the cross section of an CNT is equal to an eVen number N. Small and large circles in the figure Link fig. 1 denote two sets of atomic strings offset from each other along the z axis by a distance $\rho/2$. The diameter of the NTC is $D = a/\sin(\ pi/N)$. d is the equilibrium distance between the walls of neighboring CNTs. Then $A = D + d$ is the distance between the centers of the neighboring CNTs. In the geometry considered, carbon atoms have two degrees of freedom and can only move in the xy plane.

The atoms in the calculation cell are numbered with three indices: $i = 1, ..., I$ and $j = 1, ..., J$ are the CNT indices in the beam, they number the rows and the columns of the CNT; the index $n = 1, ..., N$ numbers the atoms inside the CNT. The total number of atoms in a cell is equal to $L = I \times J \times N$.

The total energy of the CNT forest includes four terms[37,38] and can be written as

$$H = K + U_{\mathrm{B}} + U_{\mathrm{A}} + U_{\mathrm{VdW}}, \tag{1}$$

where K is the kinetic energy and the other three terms in the right-hand side give the potential energy, which consists of the energy of valence bonds U_B, the energy of valence angles U_A, and the energy of van der Waals interactions U_{VdW}. All these four terms are described in Ref.[38] and we describe them here for the convenience of the reader. In Fig. 1, indices p, q, and s number nearest atoms of a CNT, f is the atom belonging to a different CNT. Atoms q and f' belong to the same CNT, but the distance between them is not less than $3a$. Then the energies in the right-hand side of Eq. (1) are calculated as follows.

Kinetic energy is

$$K = \frac{M}{2}\sum_{l=1}^{L} |\dot{\mathbf{r}}_l|^2, \tag{2}$$

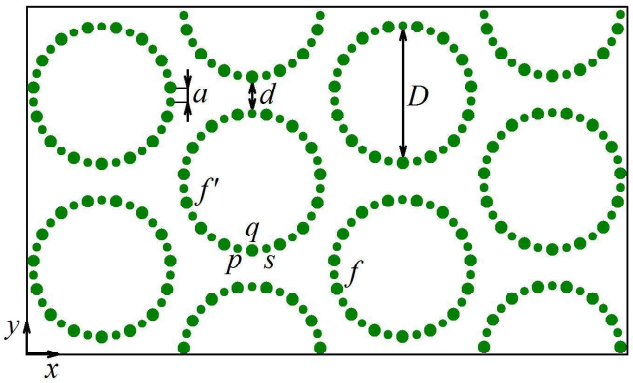

Figure 1. Calculation cell with I multiplied by J high boots (in this case $I = 4$ and $J = 2$, while in the simulation $I = 200$, $J = 8$ is used). Each zigzag CNT is represented by N carbon atoms that move along the xy plane. Shown is the case $N = 30$. Each atom denotes a rigid row of atoms perpendicular to the xy plane. Small and large circles show two types of rigid rows, offset from each other along the z axis. Here a denotes the distance between the carbon atoms in the wall of the CNT, the neighboring CNTs are separated by a distance d, D is the diameter of the CNT and $A = D + d$ is the distance between the centers of neighboring CNTs. The indices p, q, s, f and f' are used to describe the interactions between atoms (see description in the text).

where M is the carbon atom mass, $\mathbf{r}_l$ is the radius-vector of l-th atom, overdot means differentiation with respect to time, and summation is performed over all atoms in the system.

The energy of valence bonds is

$$U_{\mathrm{B}} = \sum_{i=1}^{I}\sum_{j=1}^{J}\sum_{q=1}^{N}\frac{\alpha}{2}(|\mathbf{r}_{i,j,q} - \mathbf{r}_{i,j,s}| - a)^2, \tag{3}$$

which is summation over the bonds connecting nearest atoms (see Fig. 1) and the number of such bonds is equal to the number of atoms in the computational cell. In Eq. (3), α is the valence bond stiffness.

The energy of valence angles is given by the anharmonic potential

$$U_{\mathrm{A}} = \sum_{i=1}^{I}\sum_{j=1}^{J}\sum_{q=1}^{N}\epsilon[1 + \cos\theta_{pqs}],$$
$$\cos\theta_{pqs} = \frac{(\mathbf{r}_{i,j,q} - \mathbf{r}_{i,j,p}, \mathbf{r}_{i,j,s} - \mathbf{r}_{i,j,q})}{|\mathbf{r}_{i,j,q} - \mathbf{r}_{i,j,p}||\mathbf{r}_{i,j,s} - \mathbf{r}_{i,j,q}|}, \tag{4}$$

where summation is over the valence angles formed by the atoms p, q, and s (see Fig. 1), and the number of such angles is equal to the number of atoms in the computational cell.

The energy of van der Waals interactions is described by the (5,11) Lennard-Jones potential

$$U_{\mathrm{VdW}} = \frac{1}{2}\sum_{q,f=1;\,q\neq f}^{N}\frac{\varepsilon}{6}\left[5\left(\frac{\sigma}{|\mathbf{r}_q - \mathbf{r}_f|}\right)^{11} - 11\left(\frac{\sigma}{|\mathbf{r}_q - \mathbf{r}_f|}\right)^{5}\right]. \tag{5}$$

Here, the summation is performed on all the interatomic bonds connecting the atoms q and f belonging to different CNTs, and the atoms s and f' belonging to the same CNT (see Fig. **??**). The cutoff radius for van der Waals interactions is 6 Å. As already mentioned, bonds shorter than $3a$ are not taken into account for atoms s and f' belonging to the same CNT.

The units of time, energy and distance in our simulations are picoseconds, eV and angstroms, respectively. In these units, the mass of the carbon atom in the equation (2) is $M = 12 \times 1.0364 \times 10^{-4}$ eV/ps^2 Å^2 ... The stiffness of the valence bond in the equation (3) is $\alpha = 405$ N/m,[37] which in units accepted here gives $\alpha = 25,279$ eV/Å^2. The stiffness of the bond angle in the equation (4) is $\varepsilon = 3.50$ eV.[37] The parameters Eq. (5) are $\varepsilon = 0.00166$ eV and $\sigma = 3.61$ Å.

3. SIMULATION SETUP

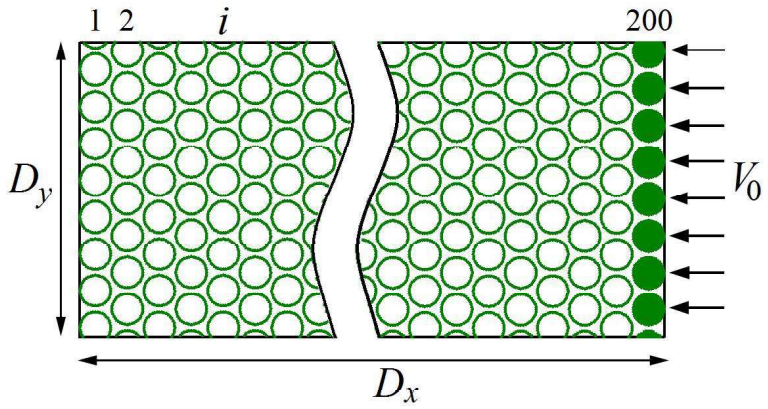

Figure 2. A calculation cell with the dimensions D_x and D_y is used to simulate the shock loading. The cell has 200 vertical rows of CNTs and 8 CNTs in each row. Vertical lines are numbered with the index $i = 1, ..., 200$. CNTs are parallel to the z axis, and their transverse compression is considered under plane strain conditions. The CNT centers create a triangular network in the xy plane. Periodic boundary conditions are applied along the y axis. The free area is on the left side of the calculation cell. The vertical row at the right end of the cell ($i = 200$) at the initial time $t = 0$ begins to move to the left with constant speed V_0 as a solid body (represented by filled circles).

Table 1. A brief description of the geometric parameters of the calculation cells used in the simulation. Here N is the number of atoms in the cross section of the CNT, D is the diameter of the CNT, A (Å) is the distance between the centers of the CNTs, D_x and D_y are the dimensions of the compute cell along the x and y axes, L is the total number of atoms.

N	30	35	40	45
D (Å)	11.75	13.7	15.65	17.6
A (Å)	14.83	16.78	18.74	20.7
D_x (Å)	2600	3000	3300	3600
D_y (Å)	120	140	150	170
L	48000	56000	64000	72000

In this study, the uniaxial compressive dynamic load of CNT beams is analyzed under plane strain conditions, as schematically shown in Fig. 2. The calculation cell has 200 vertical rows of CNTs numbered $i = 1, ..., 200$, and each row has eight CNTs numbered $j = 1, ..., 8$. Periodic boundary conditions are applied in the direction y. This structure initially relaxes at zero temperature assuming that there are free surfaces at the left and right ends of the design cell and that no external force is applied. So the equilibrium sizes of the cells i.e. D_x and D_y are after relaxation.

The table 1 shows the geometric equilibrium parameters of the calculation cells for different numbers of atoms representing the cross section of the CNTs: $N = 30$, 35, 40 and 45. These results are obtained by taking account of the interatomic distance equilibrium in graphene $\rho = 1418$ Å. The equilibrium distance between rigid atomic rows oriented along the z axis is $a = \rho\sqrt{3}/2 = 1,228$ Å.

At the initial instant $t = 0$, the rigid piston (vertical rank of NTC $i = 200$) begins to move to the left with a speed of V_0. This line is illustrated in Fig. 2 filled circles illustrating CNTs. The free surface conditions at the left end of the computational cell are preserved and simulation continues until the disturbance of the moving piston reaches the left end of the cell. The piston speeds considered in this study are of the order of 1 - 12 Å/ps (100 - 1200 m/s).

4. NUMERICAL RESULTS

The simulation of the shock compression loading of a CNT forest shows that immediately after the piston begins to move at $t = 0$, the front of the compression wave begins to propagate with a velocity of V_1; behind the front of this wave, the shape of the cross section of the CNT changes from circular to elliptical. If the piston speed exceeds the threshold value $V_0^* = 6$ Å/ps, then the second compression wave is initiated, moving with the speed $V_2 < V_1$, and behind this wave the cross sections CNT are destroyed.

Fig. 3 shows how the speed of two wave fronts (V_1 and V_2) depends on the speed of the piston V_0 for forests containing CNTs of different diameters. Two different shock wave propagation scenarios are clearly visible for low and high piston speeds with a threshold value of around $V_0^* = 6$ Å/ps, regardless of the diameter of the NTC. In scenario (1), for $V_0 < V_0^*$, the front propagation velocity of the first wave V_1 increases linearly with increasing piston velocity V_0, and the wave d collapse is not generated at all. In scenario (2), for $V_0 > V_0^*$, the speed V_1 does not depend on V_0, but at the same time, V_2 starts to increase linearly with increasing speed of the piston. In this case, the velocity V_2 shows no dependence on the diameter of the CNT, while V_1 decreases with increasing N. In addition, the speed of the wavefront V_1 for the large diameter CNTs does not change as much with an increase in the speed of the piston V_0 as for the smaller diameter CNTs. As a result, saturation can be expected for large diameters of NTC, when the speed V_1 practically ceases to depend on V_0.

Fig. 4(a) shows the displacement of the centers of gravity of CNTs in the i-th vertical row (averaged over each vertical row) for two piston velocities, V_0=3 and V_0=10 Å/ps. The results in Fig. 4(a) are presented for a time interval from 5 to 45 ps. In the top panel, propagation of the compressive waves with the speed V_1 is clearly seen. Before the wave front approaches, the centers of gravity have zero displacements. After passing the front, elliptized CNTs move with an almost constant velocity $V_1 = 61.7$ Å/ps. An increase of the piston velocity up to $V_0 = 10$ Å/ps, see bottom panel, results in an appearance of two compressive waves. The faster wave of elliptization moves with velocity of $V_1 = 67.3$ Å/ps, while the slower wave of CNT collapse with $V_2 = 21.1$ Å/ps, this fact is clearly seen by the presence of two different slopes of the displacement curves.

The characteristic ellipticity of the CNTs as a function of the vertical row number i for $V_0 = 3$ Å/ps is displayed on the top panel of figure 4(b). The ratio of the minimum diameter to the maximum diameter of the CNTs $D_{\min}/D_{\max}$ is averaged over 8 CNTs for each row. Before the start of the compression wave, the ratio $D_{\min}/D_{\max}$ is close to unity, which indicates that the cross sections of the CNTs keep their circular shape. When the wave front arrives and passes, this ratio drops rapidly to a plateau at around 0.95 and after a while

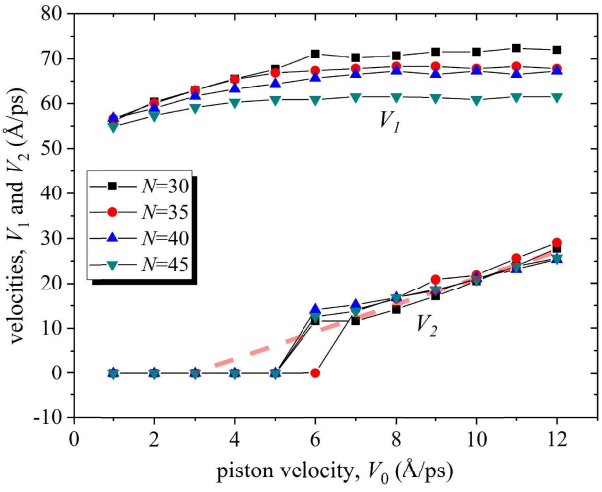

Figure 3. Dependence of the speeds of the first and second compression wave fronts, V_1 and V_2, on the speed of the piston V_0 for different diameters of CNTs (different number of atoms N in the cross section of the CNTs). A wave propagating with a speed V_1 changes the cross sections of the NTCs from circular to elliptical, and behind a wave propagating with a speed V_2, the NTCs are destroyed. The dotted line shows the linear relationship between V_2 and V_0 and serves as a guide for the eyes.

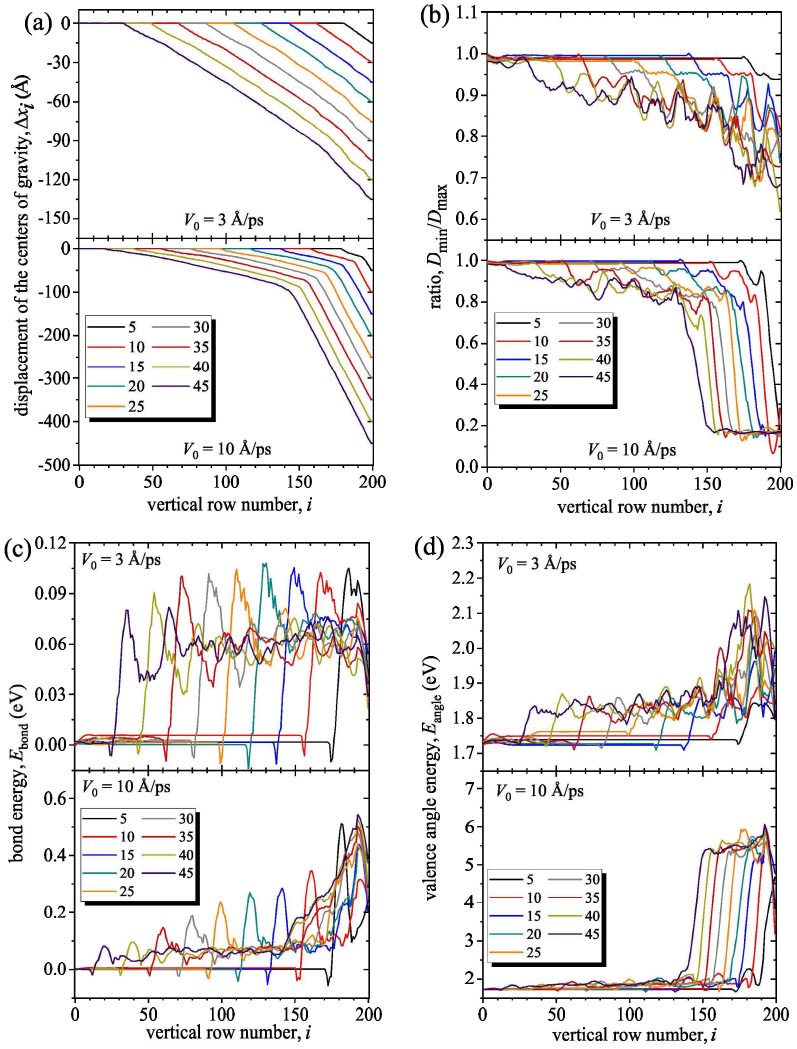

Figure 4. Distribution of structural and energy parameters along the CNT forest during the propagation of compression waves at times of 5 to 45 ps with a step of 5 ps. The parameters are averaged over eight CNTs belonging to the ith vertical row, $i = 1, ..., 200$. (a) displacement of the centers of gravity of the CNTs along the axis x; (b) ellipticity of the CNTs, ie the ratio between the minimum diameter of the CNTs and the maximum diameter; (c) modify the energies of the bond $E_{\rm bond}$; and (d) modifying the energies of the bond angle $E_{\rm angle}$. The upper panels of each subfigure show the results for piston speed $V_0 = 3$ Å/ps, and the lower panels for $V_0 = 10$ Å/ps. In both cases, $N = 40$.

decreases, creating new fluctuations. The minimum value of the coefficient observed in this numerical analysis is approximately 0.65. At higher piston speed, $V_0 = 10$ Å/ps (see bottom panel), after the elliptical wavefront has passed, a decrease of $D_{\rm min}/D_{\rm max}$ is observed at around 0.8 . However, as the collapse wave passes, the ratio $D_{\rm min}/D_{\rm max}$ drops sharply to around 0.2. It is this value which characterizes CNTs completely destroyed in the forest.

Potential energy per atom (averaged over eight CNTs for each row) stored by valence bonds and valence angles are presented in Fig. 4(c) and (d), respectively. As seen, before the wave comes, CNTs have nearly zero valence bond energy and valence angle energy of about 1.75 eV. This energy is attributed to the energy spent to bend flat graphene sheets into CNTs. Passing of the elliptization compressive wave increases $E_{\rm bond}$ up to about 0.06 eV and $E_{\rm angle}$ up to about 1.85 eV. The subsequent collapse wave increases the energy significantly, $E_{\rm bond}$

up to 0.5 eV on average and E_{angle} up to 5.5 eV. It should be noted that some time is needed for elliptization of CNTs in the forest after passing the elliptization wave. Elliptization results in further increase of E_{angle} up to the values of 2.05 eV. The front of CNT elliptization can also be seen in Fig. 4(d), namely, behind the front the ratio $D_{\min}/D_{\max}$ is higher than before the front (see Fig. 4(b)).

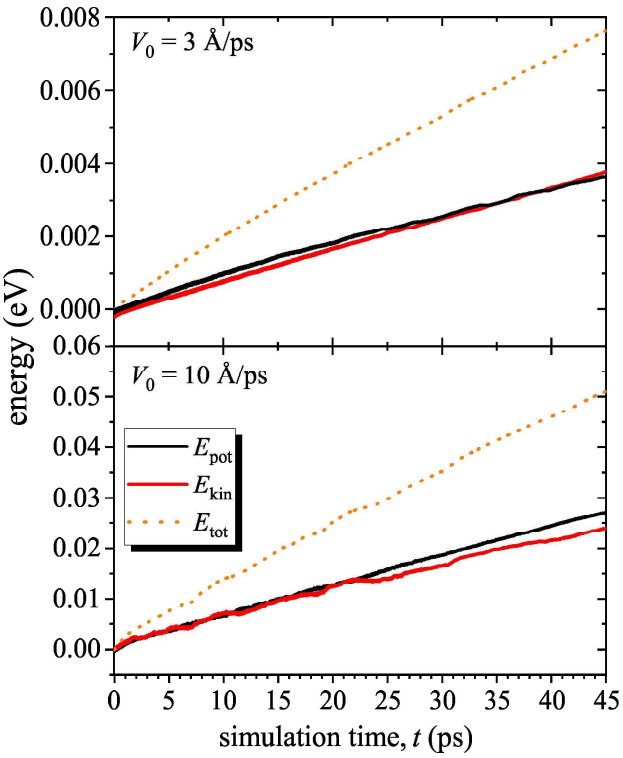

Figure 5. The energies per particle of the entire computational cell as functions of time. In (a) kinetic, potential and total energies are presented. In (b) the three components of potential energy are plotted: the energy of Van der Waals interactions (black line), the energy of valence bonds (red line), and the energy of valence angles (blue line). Upper panel of each subfigure contains results for the piston speed of V_0=3 Å/ps and lower panel for V_0=10 Å/ps. For both cases N=40.

5. DISCUSSION AND CONCLUSIONS

Thus, the propagation of a compression wave in a single-walled CNT forrest was studied using a chain model with a reduced number of degrees of freedom. Depending on the speed of the piston, two different scenarios of shock wave propagation and their influence on the structure of the CNT forrest have been identified. At values above the threshold, two compression waves were observed: (1) a faster wave front leading to elliptization of the CNT cross sections, and (2) and a slower collapsing wave front that followed some time later. At values below the threshold value, only the wave front (1) was detected. The energy absorption by a CNT forest is much higher in the case of a CNT collapse and occurs due to an increase in the energy of the bond angles. The rate of absorption of shock wave energy increases with increasing piston speed. This latter result can be useful when designing elastic shock absorbers.

In this study, only single-walled CNTs of the same diameter were considered. As CNTs often have double and triple walls and there is always a dispersion of diameters in the forest, the study of the absorption of shock wave energy in such systems seems to be a natural continuation of this work.

Acknowledgements

For A.M.B. and S.V.D. this work was carried out with financial support from the Russian Science Foundation, grant no. 21-19-00813 (obtaining results, writing manuscript), I.A.S. acknowledges the financial support of the Council of the President of the Russian Federation for state support of young Russian scientists, grant No. MK-815.2020.2 (analysis of the results).

REFERENCES

[1] Treacy, M.M.J.; Ebbesen, T.W.; Gibson, J.M. Exceptionally high Young's modulus observed for individual carbon nanotubes. *Nature* **1996** *381*, 678–680.

[2] Wong, E.W.; Sheehan, P.E.; Lieber, C.M. Nanobeam mechanics: Elasticity, strength, and toughness of nanorods and nanotubes. *Science* **1997** *277*, 1971–1975.

[3] Hecht, D.S.; Hu, L.; Irvin, G. Emerging transparent electrodes based on thin films of carbon nanotubes, graphene, and metallic nanostructures. *Advanced Materials* **2011** *23*, 1482–1513.

[4] Popov, V.N. Carbon nanotubes: Properties and application. *Materials Science and Engineering R: Reports* **2004** *43*, 61–102.

[5] Katin,K.P. ; Maslov, M.M.; Krylov, K.S.; Mur, V.D. On the impact of substrate uniform mechanical tension on the graphene electronic structure. *Materials* **2020** *13*, 4683.

[6] Li, M.; Mu, B. Effect of different dimensional carbon materials on the properties and application of phase change materials: A review. *Applied Energy* **2019** *242*, 695–715.

[7] Biercuk, M.J.; Llaguno, M.C.; Radosavljevic, M.; Hyun, J.K.; Johnson, A.T.; Fischer, J.E. Carbon nanotube composites for thermal management. *Applied Physics Letters* **2002** *80*, 2767–2769.

[8] Li, Y.; Huang, X.; Zeng, L.; Li, R.; Tian, H.; Fu, X.; Wang, Y.; Zhong, W.-H. A review of the electrical and mechanical properties of carbon nanofiller-reinforced polymer composites. *Journal of Materials Science* **2019** *54*, 1036–1076.

[9] Chawla, R.; Sharma, S. Molecular dynamics simulation of carbon nanotube pull-out from polyethylene matrix. *Composites Science and Technology* **2017** *144*, 169–177.

[10] Chen, X.; Paul, R.; Dai, L. Carbon-based supercapacitors for efficient energy storage. *National Science Review* **2017** *4*, 453–489.

[11] Afzal, A.; Abuilaiwi, F.A.; Habib, A.; Awais, M.; Waje, S.B.; Atieh, M.A. Polypyrrole/carbon nanotube supercapacitors. Technological advances and challenges. *Journal of Power Sources* **2017** *352*, 174–186.

[12] Wang, B.; Huang, W.; Chi, L.; Al-Hashimi, M.; Marks, T.J.; Facchetti, A. High- k gate dielectrics for emerging flexible and stretchable electronics. *Chemical Reviews* **2018** *118*, 5690–5754.

[13] Tornabene, F.; Fantuzzi, N.; Bacciocchi, M. Linear static response of nanocomposite plates and shells reinforced by agglomerated carbon nanotubes. *Composites Part B: Engineering* **2017** *115*, 449–476.

[14] Islam, S.; Saleh, T.; Asyraf, M.R.M.; Mohamed Ali, M.S. An ex-situ method to convert vertically aligned carbon nanotubes array to horizontally aligned carbon nanotubes mat. *Mater. Res. Express* **2019**, *6*, 025019.

[15] Zhang, R.; Zhang, Y.; Wei, F. Horizontally aligned carbon nanotube arrays: Growth mechanism, controlled synthesis, characterization, properties and applications. *Chem. Soc. Rev.* **2017**, *46*, 3661–3715.

[16] Nam, T.H.; Goto, K.; Yamaguchi, Y.; Premalal, E.V.A.; Shimamura, Y.; Inoue, Y.; Naito, K.; Ogihara, S. Effects of CNT diameter on mechanical properties of aligned CNT sheets and composites. *Compos. Part A Appl. Sci. Manuf.* **2015**, *76*, 289–298.

[17] Qiu, L.; Wang, X.; Su, G.; Tang, D.; Zheng, X.; Zhu, J.; Wang, Z.; Norris, P.M.; Bradford, P.D.; Zhu, Y. Remarkably enhanced thermal transport based on a flexible horizontally-aligned carbon nanotube array film. *Sci. Rep.* **2016**, *6*, 21014.

[18] Tang, J.; Sasaki, T.; Yudasaka, M.; Matsushita, A.; Iijima, S. Compressibility and polygonization of single-walled carbon nanotubes under hydrostatic pressure. *Phys. Rev. Lett.* **2000**, *85*, 1887–1889.

[19] Karmakar, S.; Sharma, S.M.; Teredesai, P.V.; Muthu, D.V.S.; Govindaraj, A.; Sikka, S.K.; Sood, A.K. Structural changes in single-walled carbon nanotubes under non-hydrostatic pressures: X-ray and Raman studies. *New J. Phys.* **2003**, *5*, 143.1–143.11.

[20] Qian, D.; Wagner, G.J.; Liu, W.K.; Yu, M.-F.; Ruoff, R.S. Mechanics of carbon nanotubes. *Appl. Mech. Rev.* **2002**, *55*, 495–532.

[21] Silva-Santos, S.D.; Alencar, R.S.; Aguiar, A.L.; Kim, Y.A.; Muramatsu, H.; Endo, M.; Blanchard, N.P.; San-Miguel, A.; Souza Filho, A.G. From high pressure radial collapse to graphene ribbon formation in triple-wall carbon nanotubes. *Carbon* **2019**, *141*, 568–579.

[22] Tangney, P.; Capaz, R.B.; Spataru, C.D.; Cohen, M.L.; Louie, S.G. Structural transformations of carbon nanotubes under hydrostatic pressure. *Nano Lett.* **2005** *5*, 2268–2273.

[23] Zhang, S.; Khare, R.; Belytschko, T.; Hsia, K.J.; Mielke, S.L.; Schatz, G.C. Transition states and minimum energy pathways for the collapse of carbon nanotubes. *Phys. Rev. B* **2006**, *73*, 075423.

[24] Shima, H.; Sato, M. Multiple radial corrugations in multiwalled carbon nanotubes under pressure. *Nanotechnology* **2008**, *19*, 495705.

[25] Zhao, Z.S.; Zhou, X.-F.; Hu, M.; Yu, D.L.; He, J.L.; Wang, H.-T.; Tian, Y.J.; Xu, B. High-pressure behaviors of carbon nanotubes. *J. Superhard Mater.* **2012**, *34*, 371–385.

[26] Baimova, J.A.; Dmitriev, S.V.; Zhou, K. Strain-induced ripples in graphene nanoribbons with clamped edges. *Phys. Status Solidi B* **2012** *249*, 1393–1398.

[27] Lee, J.H.; Loya, P.E.; Lou, J.; Thomas, E.L. Dynamic mechanical behavior of multilayer graphene via supersonic projectile penetration. *Science* **2014** *346*, 1092–1096.

[28] Yoon, K.; Ostadhossein, A.; Van Duin, A.C.T. Atomistic-scale simulations of the chemomechanical behavior of graphene under nanoprojectile impact. *Carbon* **2016** *99*, 58–64.

[29] Haque, B.Z.; Chowdhury, S.C.; Gillespie, J.W. Molecular simulations of stress wave propagation and perforation of graphene sheets under transverse impact. *Carbon* **2016** *102*, 126–140.

[30] Hosseini-Hashemi, S.; Sepahi-Boroujeni, A.; Sepahi-Boroujeni, S. Analytical and molecular dynamics studies on the impact loading of single-layered graphene sheet by fullerene. *Appl. Surf. Sci.* **2018** *437*, 366–374.

[31] Yang, L.; Tong, L. Suspended monolayer graphene traps high-speed single-walled carbon nanotube. *Carbon* **2016** *107*, 689–695.

[32] Shepelev, I.A.; Chetverikov, A.P.; Dmitriev, S.V.; Korznikova, E.A. Shock waves in graphene and boron nitride. *Comp. Mater. Sci.* **2020** *177*, 109549.

[33] Noël, M.; Ananev, S.; Mases, M.; Devaux, X.; Lee, J.; Evdokimov, I.; Dossot, M.; Mcrae, E.; Soldatov, A.V. Probing structural integrity of single walled carbon nanotubes by dynamic and static compression. *Physica Status Solidi - Rapid Research Letters* **2014** *8*, 935–938.

[34] Lahiri, D.; Das, S.; Choi, W.; Agarwal, A. Unfolding the damping behavior of multilayer graphene membrane in the low-frequency regime. *ACS Nano* **2012** *6*, 3992–4000.

[35] Liu, X.; Wang, F.; Wu, H.; Wang, W. Strengthening metal nanolaminates under shock compression through dual effect of strong and weak graphene interface. *Applied Physics Letters* **2014** *104*, 231901.

[36] Bizao, R.A.; Machado, L.D.; De Sousa, J.M.; Pugno, N.M.; Galvao, D.S. Scale effects on the ballistic penetration of graphene sheets. *Scientific Reports* **2018** *8*, 6750.

[37] Savin, A.V.; Korznikova, E.A.; Dmitriev, S.V. Scroll configurations of carbon nanoribbons. *Phys. Rev. B* **2015**, *92*, 035412.

[38] Korznikova, E.A.; Rysaeva, L.K.; Savin, A.V.; Soboleva, E.G.; Ekomasov, E.G.; Ilgamov, M.A.; Dmitriev, S.V. Chain model for carbon nanotube forest under plane strain conditions. *Materials* **2019**, *12*, 3951.